A New Parameterization of the Accretion of Cloud Water by Snow and Its Evaluation through Simulations of Mesoscale Convective Systems

HAN-GYUL JIN AND JONG-JIN BAIK

School of Earth and Environmental Sciences, Seoul National University, Seoul, South Korea

(Manuscript received 28 November 2019, in final form 12 June 2020)

ABSTRACT

A new parameterization of the accretion of cloud water by snow for use in bulk microphysics schemes is derived as an analytic approximation of the stochastic collection equation (SCE), where the theoretical collision efficiency for individual snowflake–cloud droplet pairs is applied. The snowflake shape is assumed to be nonspherical with the mass–size and area–size relations suggested by an observational study. The performance of the new parameterization is compared to two parameterizations based on the continuous collection equation, one with the spherical shape assumption for snowflakes (SPH-CON), and the other with the nonspherical shape assumption employed in the new parameterization (NSP-CON). In box model simulations, only the new parameterization reproduces a relatively slow decrease in the cloud droplet number concentration, which is predicted by the direct SCE solver. This results from considering the preferential collection of cloud droplets depending on their sizes in the new parameterization based on the SCE. In idealized squall-line simulations using a cloud-resolving model, the new parameterization predicts heavier precipitation in the convective core region compared to SPH-CON, and a broader area of the trailing stratiform rain compared to NSP-CON due to the horizontal advection of greater amount of snow in the upper layer. In the real-case simulations of a line-shaped mesoscale convective system that passed over the central Korean Peninsula, the new parameterization predicts higher frequencies of light precipitation rates and lower frequencies of heavy precipitation rates. The relatively large amount of upper-level snow in the new parameterization contributes to a broadening of the area with significant snow water path.

1. Introduction

The accretion process is a cloud microphysical process that plays a major role in the growth of ice particles in mixed-phase clouds. In the dry-growth regime of ice particles, supercooled droplets colliding with an ice particle at temperatures below 0°C are accreted by the ice particle as they immediately freeze after collision (Wang and Ji 2000; Lamb and Verlinde 2011); this growth of the ice particles is also called the riming process. As the mass and dimension of an ice particle increase, the area swept by the particle and the terminal velocity of the particle also increase in general, and the ice particle becomes capable of collecting supercooled droplets more efficiently. Eventually, an ice particle that has grown enough to overcome in-cloud updrafts falls to reach the surface or meets the melting layer and reaches the surface in the form of a raindrop. In cloud models, precipitating ice particles are commonly classified into snowflakes, graupel particles, and hailstones. Because the characteristics of these three ice hydrometeor types greatly differ from each other, the precipitation characteristics may vary significantly depending on the growth of each hydrometeor type by the accretion process (e.g., Wang and Georgakakos 2005; Morrison and Milbrandt 2011). Therefore, parameterizations for the accretion process that yield good performance should be used in cloud models for better precipitation predictions.

In recent years, several cloud microphysics models with improved treatments of ice microphysics have been developed. Morrison and Milbrandt (2015) developed the predicted particle properties (P3) scheme, a bulk microphysics scheme in which the physical properties of ice particles such as the rimed mass and rimed volume are prognosed in addition to the total mass and number concentrations that have been originally considered in double-moment microphysics schemes. Jensen et al. (2017) presented the Ice-Spheroids Habit Model with Aspect-Ratio Evolution (ISHMAEL), a bulk microphysics scheme that predicts the evolution of the aspect ratio, size, and density as well as the mass and number of

Corresponding author: Jong-Jin Baik, jjbaik@snu.ac.kr

DOI: 10.1175/JAS-D-19-0326.1

ice particles approximating the ice particle shape as spheroids. Most recently, Brdar and Seifert (2018) developed the Monte Carlo ice microphysics model (McSnow), a Lagrangian superparticle model that predicts the ice mass, rime mass, rime volume, and monomer number for each Lagrangian superparticle. The novel cloud microphysics models take into account additional prognostic variables for ice hydrometeors and therefore manage to better represent the complex evolution of ice particle properties in clouds. In virtue of the explicit prediction of the evolution of ice particle properties, these models do not use fixed ice hydrometeor types with fixed particle properties.

Despite these improvements in representing ice-phase microphysics, bulk microphysics schemes still need (and have room for) additional improvements, especially in terms of the parameterization of the accretion process. In most bulk microphysics schemes, the accretion of cloud water by ice hydrometeors is parameterized based on the simple continuous collection equation or a simplified stochastic collection equation (SCE) considering the bulk collection efficiency (Milbrandt and Yau 2005; Hong and Lim 2006; Thompson et al. 2008; Lim and Hong 2010). The bulk collection efficiency is a collection efficiency representative of the two colliding hydrometeor species and is expressed as a constant value or determined by the two mean sizes of the colliding hydrometeor species. The use of the bulk collection efficiency simplifies the solution of the SCE, but has several problems. Most of the theoretically or numerically obtained collection efficiencies employed as references for the bulk collection efficiency is the collection efficiency between two individual colliding particles (e.g., Wang and Ji 2000). If this collection efficiency is approximated into the bulk collection efficiency as a function of the two mean particle sizes of the colliding hydrometeor species, a large bias can be generated depending on the various particle size distributions. Considering the problem of using the bulk collection efficiency, Jin et al. (2019) developed a parameterization of the accretion of cloud water by graupel derived as an analytic approximation of the SCE using the collection efficiency of individual graupel particle–cloud droplet pairs. They found that this approach complicates the parameterization to some extent, but yields more realistic predictions of the changes in the mass and number concentrations of the hydrometeor species via the accretion process compared to the approach using the bulk collection efficiency.

Using a similar approach to that of Jin et al. (2019), this study develops a new parameterization of the accretion of cloud water by snow and evaluates the parameterization through cloud and precipitation simulations. Although a high uncertainty exists in the assumption of the snowflake shape that is almost inevitable in conventional bulk microphysics schemes, a reasonable parameterization can be obtained assuming the mass–size and area–size relationships for snowflakes that are based on in situ observations, rather than using the traditional constant-density sphere assumption for the snowflake shape.

In this study, a new parameterization of the accretion of cloud water by snow for use in bulk microphysics schemes is derived as an analytic approximation of the SCE. The derivation of the new parameterization is given in section 2. In section 3, the performance of the new parameterization is evaluated through box model simulations. In section 4, the effects of the new parameterization are evaluated through cloud-resolving simulations of idealized and real-case precipitating systems. A summary and conclusions are given in section 5.

2. Derivation of a new accretion parameterization

The rate of change in the snow mass content L_s via accretion of cloud droplets is given by the SCE, which is also applicable for collection between other species (e.g., Verlinde et al. 1990):

$$\left.\frac{\partial L_s}{\partial t}\right|_{\text{acc}} = \frac{4}{3}\pi\rho_w \int_0^\infty \int_0^\infty r^3 f_s(R) K(R,r) f_c(r)\, dr dR. \tag{1}$$

Here, ρ_w is the density of liquid water; r is the radius of cloud droplets; R is one-half of the maximum dimension D_m of snowflakes; K is the collection kernel; and f_s and f_c are the size distribution functions of snowflakes and cloud droplets, respectively. It is noted that small-scale stochastic fluctuations in the size distributions and collection kernel are not considered in (1), which makes the SCE not fully stochastic. The size distribution functions f_s and f_c are expressed by three-parameter gamma distribution functions:

$$f_s(R) = N_{0,s} R^{\mu_s} \exp(-\lambda_s R), \tag{2a}$$

$$f_c(r) = N_{0,c} r^{\mu_c} \exp(-\lambda_c r), \tag{2b}$$

where $N_{0,s}$ and $N_{0,c}$ are the intercept parameters; μ_s and μ_c are the shape parameters; and λ_s and λ_c are the slope parameters. Several airborne measurement studies have shown that the snowflake size distributions in reality can be effectively described by the classic exponential function (Houze et al. 1979; Woods et al. 2008), which corresponds to $\mu_s = 0$. For the numerical simulations in the following sections, μ_s is preset to 0, while μ_c is diagnosed by the empirical relation of Thompson et al. (2008), $\mu_c = \min[15, \text{nint}(10^9/N_c + 2)]$. Here, N_c is the

total number concentration of cloud droplets (m^{-3}) and nint(x) refers to the nearest integer of x.

The collection kernel K is given by

$$K(R,r) = A_{sw}(R,r)\left|v_{t,s}(R) - v_{t,c}(r)\right|\eta(R,r), \quad (3)$$

where A_{sw} is the geometric sweep-out area; $v_{t,s}$ and $v_{t,c}$ are the terminal velocities of snowflakes and cloud droplets, respectively; and η is the collection efficiency. To evaluate these variables, the mass–size and area–size relations of snowflakes must be prescribed. A widely used assumption to obtain these relations is that the snowflakes have a spherical shape with a constant bulk density (e.g., 100 kg m^{-3}) (Lin et al. 1983; Lim and Hong 2010). However, in reality, the bulk density of snowflakes varies considerably, generally decreasing with an increase in the snowflake size (Heymsfield et al. 2004; Brandes et al. 2007; Molthan et al. 2010). An alternative is to describe the mass–size and area–size relations of snowflakes as $m_s = \alpha R^{\beta}$ and $A_s = \gamma R^{\delta}$, respectively, using the fractal dimensions β and δ, where β and δ are not restricted to 3 and 2, respectively (Locatelli and Hobbs 1974; Mitchell 1996). Here, m_s is the mass of snowflakes and A_s is the cross-sectional area of snowflakes perpendicular to its fall direction. In this study, empirical mass–size and area–size relations estimated from aircraft- and balloon-borne observation data in midlatitude clouds provided by Heymsfield (2003) are used, where $\alpha = 0.9778$ kg $m^{-\beta}$, $\beta = 2.25$, $\gamma = 0.1684$ $m^{2-\delta}$, and $\delta = 1.67$. The adopted mass–size relation gives intermediate values of the snowflake mass between the two commonly used quadratic mass–size relations, namely, $m_s = 0.038D_m^2$ (Baldauf et al. 2011; Seifert et al. 2014) and $m_s = 0.069D_m^2$ (Field et al. 2005; Thompson et al. 2008), in the snowflake size range of $1.2 < D_m < 12$ mm, which encompasses most of the typical size range of snowflakes. The adopted area–size relation gives greater values of the snowflake cross-sectional area than the empirical area–size relation for unrimed aggregates, $A_s = 0.1315D_m^{1.88}$ (Mitchell 1996), for $D_m < 14$ mm.

Once the mass–size and area–size relations for snowflakes have been described, the terminal velocity relation can be obtained by a theoretical approach using the boundary layer theory (Böhm 1989; Mitchell 1996; Khvorostyanov and Curry 2002, 2005; Mitchell and Heymsfield 2005). The analytical expression for the terminal velocity suggested by Khvorostyanov and Curry (2005) is valid for a wide range of snowflake sizes by taking the effect of turbulence into consideration. A gamma-type fitted function for the terminal velocity of snowflakes $v_{t,s} = v_{0,s}R^{c_1}\exp(-c_2R)$, where the values of $v_{0,s}$, c_1, and c_2 are 79.83 m^{1-c_1} s^{-1}, 0.611, and 77.33 m^{-1}, respectively, is obtained by employing the analytical expression of Khvorostyanov and Curry (2005) as the reference (Fig. 1). The fitted terminal velocity agrees well with the reference for the typical size range of snowflakes; the deviation from the reference does not exceed ± 0.15 m s^{-1}. For the terminal velocity of cloud droplets, the power-law fitted function $v_{t,c} = v_{0,c}r^2$ ($v_{0,c} = 1.0973 \times 10^8$ m^{-1} s^{-1}) for the empirical relation of Beard (1976) is used as in Lee and Baik (2017) and Jin et al. (2019). The terminal velocities of snowflakes and cloud droplets are multiplied by the density factor $(\rho_0/\rho)^{1/2}$ to consider the increase in the terminal velocity when the air density decreases. Here, ρ_0 denotes the reference air density.

In the collision between two spherical particles, the geometric sweep-out area A_{sw} is simply given by $\pi(R + r)^2$. However, it becomes difficult to estimate A_{sw} if one of the particles has an irregular shape, such as aggregates. In this study, A_{sw} is approximated following the method of Connolly et al. (2012):

$$\begin{aligned} A_{sw} &\approx (A_s^{1/2} + A_c^{1/2})^2 \\ &= \gamma R^{\delta} + 2(\gamma\pi)^{1/2}R^{\delta/2}r + \pi r^2 \\ &= \sum_{i=0}^{2} a_i R^{(1-i/2)\delta} r^i, \end{aligned} \quad (4)$$

where A_c is the cross-sectional area of cloud droplets and a_i is given as $[a_0, a_1, a_2] = [\gamma, 2(\gamma\pi)^{1/2}, \pi]$.

To determine the collection efficiency, the collision efficiency of Böhm (1994, 1999) is adopted, assuming that a cloud droplet colliding with a snowflake is always collected by the snowflake (i.e., the coalescence efficiency is 1, where the collection efficiency is the product of the collision efficiency and the coalescence efficiency). Böhm (1994, 1999) calculated the collision efficiency between two particles based on the boundary layer theory. Because various sizes and shapes of the colliding particles can be considered in the method of Böhm (1994, 1999), Böhm's collision efficiency has been widely used in parameterizations in recent years (Phillips et al. 2015; Brdar and Seifert 2018; Lee et al. 2019). The fitted function for Böhm's collision efficiency can be obtained as

$$\eta = b_0[1-\exp(-b_1r)][\exp(-b_2R) - \exp(-b_3R - b_4r)]. \quad (5)$$

The determined values of b_0, b_1, b_2, b_3, and b_4 are 1, 138 006 m^{-1}, 4.809 m^{-1}, 3038 m^{-1}, and 83 477 m^{-1}, respectively. Figure 2 shows the fitted collision efficiency and its deviation from Böhm's collision efficiency. The fitted collision efficiency is in good agreement with Böhm's collision efficiency in terms of both magnitude

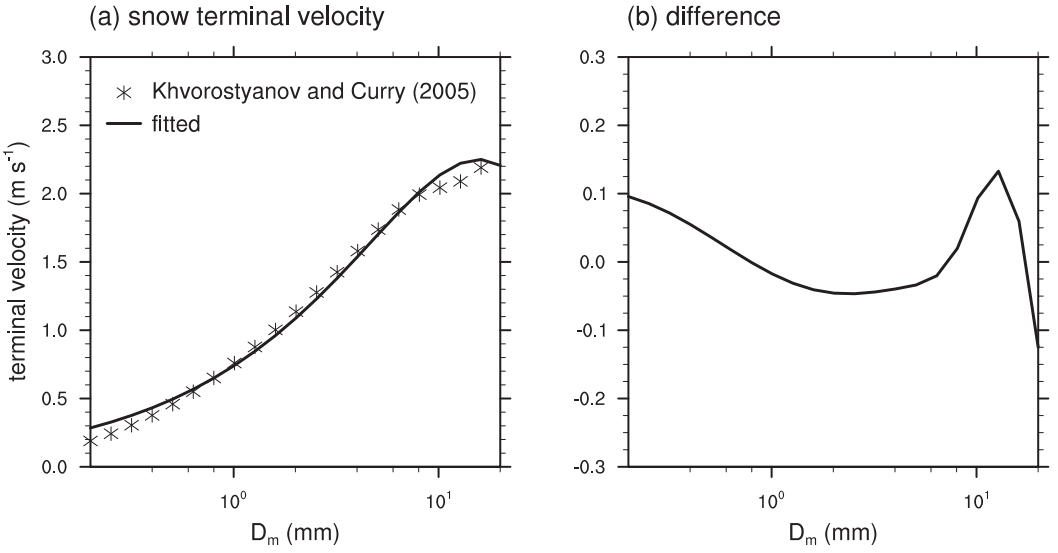

FIG. 1. (a) Terminal velocities of snowflakes obtained using the method of Khvorostyanov and Curry (2005) and the fitted function. (b) The fitted terminal velocity minus the reference terminal velocity.

and size dependency. The overestimation for very small cloud droplets ($r < \sim 6\,\mu$m) is noticeable, which means that the bulk accretion rate can be overestimated under some circumstances when the mean cloud droplet size is very small.

As all components that constitute (1) have now been specified, the analytic representation for (1) can be obtained. The absolute value of the terminal velocity difference in (3), which makes the solution extremely complicated (Verlinde et al. 1990), is approximated as the terminal velocity difference itself following Gaudet and Schmidt (2005). This approximation is justified by the fact that the contribution of the portion where cloud droplets are faster than snowflakes to the bulk accretion rate is very small. Using this, the analytic representation of (1) gives the accretion rate expressed as follows:

$$\left.\frac{\partial L_s}{\partial t}\right|_{\text{acc}} = \frac{4}{3}\pi\rho_w\left(\frac{\rho_0}{\rho}\right)^{1/2} N_{0,s}N_{0,c}b_0(v_{0,s}L_1 - v_{0,c}L_2), \quad (6)$$

where

$$\begin{aligned} L_1 = \sum_{i=0}^{2} a_i \Bigg\{ & \Gamma_1\left(\lambda_s + b_2 + c_2, \mu_s + 1 + \left(1 - \frac{i}{2}\right)\delta + c_1\right) \\ & \times [\Gamma_1(\lambda_c, \mu_c + 4 + i) - \Gamma_1(\lambda_c + b_1, \mu_c + 4 + i)] \\ & - \Gamma_1\left(\lambda_s + b_3 + c_2, \mu_s + 1 + \left(1 - \frac{i}{2}\right)\delta + c_1\right) \\ & \times [\Gamma_1(\lambda_c + b_4, \mu_c + 4 + i) \\ & - \Gamma_1(\lambda_c + b_1 + b_4, \mu_c + 4 + i)]\Bigg\}, \end{aligned} \quad (7a)$$

$$\begin{aligned} L_2 = \sum_{i=0}^{2} a_i \Bigg\{ & \Gamma_1\left(\lambda_s + b_2, \mu_s + 1 + \left(1 - \frac{i}{2}\right)\delta\right) \\ & \times [\Gamma_1(\lambda_c, \mu_c + 6 + i) - \Gamma_1(\lambda_c + b_1, \mu_c + 6 + i)] \\ & - \Gamma_1\left(\lambda_s + b_3, \mu_s + 1 + \left(1 - \frac{i}{2}\right)\delta\right) \\ & \times [\Gamma_1(\lambda_c + b_4, \mu_c + 6 + i) \\ & - \Gamma_1(\lambda_c + b_1 + b_4, \mu_c + 6 + i)]\Bigg\}. \end{aligned} \quad (7b)$$

Here, δ is the fractal dimension in the area-size relation of snowflakes as defined above, and $\Gamma_1(\lambda, s)$ is defined as:

$$\Gamma_1(\lambda, s) = \frac{\Gamma(s)}{\lambda^s}, \quad (8)$$

where $s > 0$ and Γ is the gamma function. Mass conservation yields the following relation:

$$\left.\frac{\partial L_c}{\partial t}\right|_{\text{acc}} = -\left.\frac{\partial L_s}{\partial t}\right|_{\text{acc}}. \quad (9)$$

The tendency of the cloud droplet number concentration by the accretion process can be evaluated by solving the following equation:

$$\left.\frac{\partial N_c}{\partial t}\right|_{\text{acc}} = -\int_0^\infty\int_0^\infty f_s(R)K(R,r)f_c(r)\,dr dR. \quad (10)$$

Equation (10) is then represented as follows:

$$\left.\frac{\partial N_c}{\partial t}\right|_{\text{acc}} = -\left(\frac{\rho_0}{\rho}\right)^{1/2} N_{0,s}N_{0,c}b_0(v_{0,s}N_1 - v_{0,c}N_2), \quad (11)$$

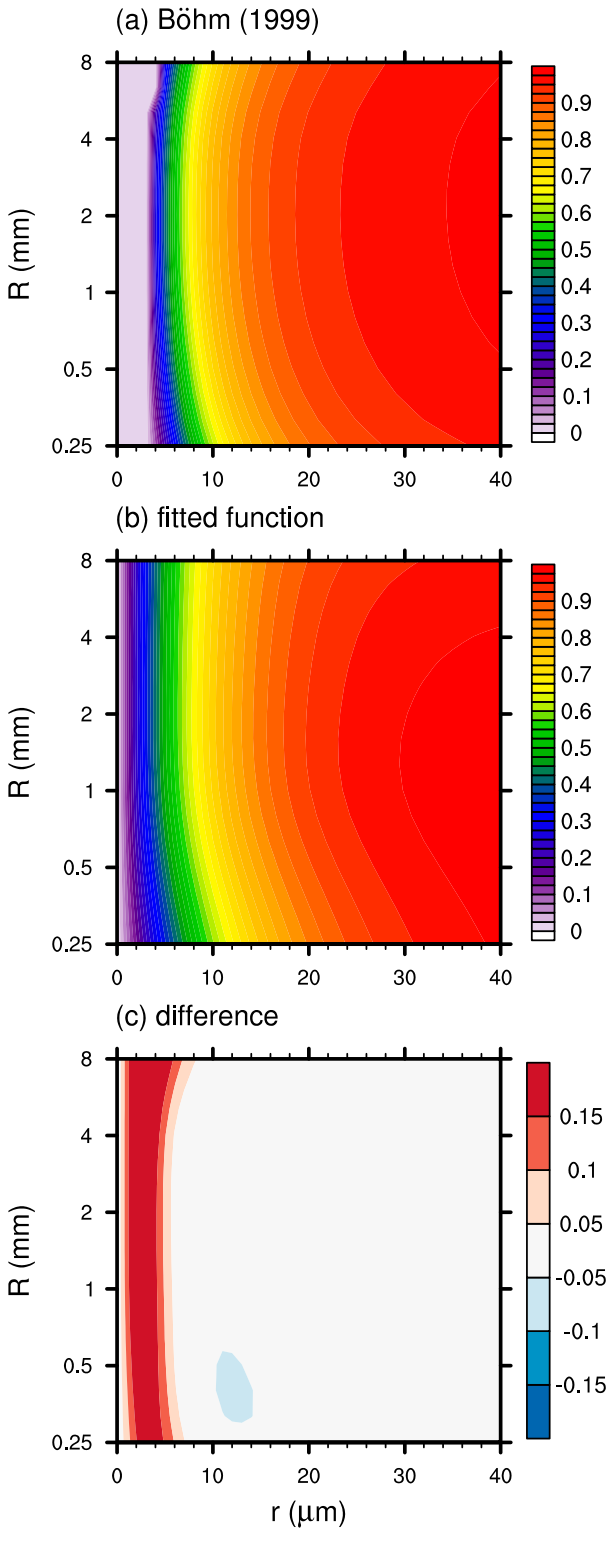

FIG. 2. (a) Collision efficiency between snowflakes and cloud droplets obtained using the method of Böhm (1999) and (b) the fitted function. (c) The fitted collision efficiency minus Böhm's collision efficiency.

where

$$N_1 = \sum_{i=0}^{2} a_i \Bigg\{ \Gamma_1\left(\lambda_s + b_2 + c_2, \mu_s + 1 + \left(1 - \frac{i}{2}\right)\delta + c_1\right) \times [\Gamma_1(\lambda_c, \mu_c + 1 + i) - \Gamma_1(\lambda_c + b_1, \mu_c + 1 + i)] - \Gamma_1\left(\lambda_s + b_3 + c_2, \mu_s + 1 + \left(1 - \frac{i}{2}\right)\delta + c_1\right) \times [\Gamma_1(\lambda_c + b_4, \mu_c + 1 + i) - \Gamma_1(\lambda_c + b_1 + b_4, \mu_c + 1 + i)] \Bigg\}, \tag{12a}$$

$$N_2 = \sum_{i=0}^{2} a_i \Bigg\{ \Gamma_1\left(\lambda_s + b_2, \mu_s + 1 + \left(1 - \frac{i}{2}\right)\delta\right) \times [\Gamma_1(\lambda_c, \mu_c + 3 + i) - \Gamma_1(\lambda_c + b_1, \mu_c + 3 + i)] - \Gamma_1\left(\lambda_s + b_3, \mu_s + 1 + \left(1 - \frac{i}{2}\right)\delta\right) \times [\Gamma_1(\lambda_c + b_4, \mu_c + 3 + i) - \Gamma_1(\lambda_c + b_1 + b_4, \mu_c + 3 + i)] \Bigg\}. \tag{12b}$$

The snowflake number concentration is not directly affected by the accretion process.

3. Box model results

A box model is designed to evaluate the new accretion parameterization. In this model, only collisions between snowflakes and cloud droplets occur, and the mass and number concentrations of snowflakes and cloud droplets are predicted. Due to the accretion process, cloud water mass is converted into snow mass as time passes.

The new parameterization is compared with other accretion parameterizations derived based on the continuous collection equation that is expressed as

$$\left.\frac{\partial L_s}{\partial t}\right|_{\text{acc}} = \frac{4}{3}\pi\rho_w L_c \overline{\eta} \int_0^\infty A_s(R) v_{t,s}(R) f_s(R)\, dR, \tag{13}$$

where $\overline{\eta}$ is the bulk collection efficiency. In this equation, the contribution of cloud droplets to the geometric sweep-out area and the terminal velocity of cloud droplets are ignored; only the bulk properties of cloud droplets (e.g., the cloud water mass and the mean size of cloud droplets if the bulk collection efficiency depends on it) contribute to the accretion rate. Although this

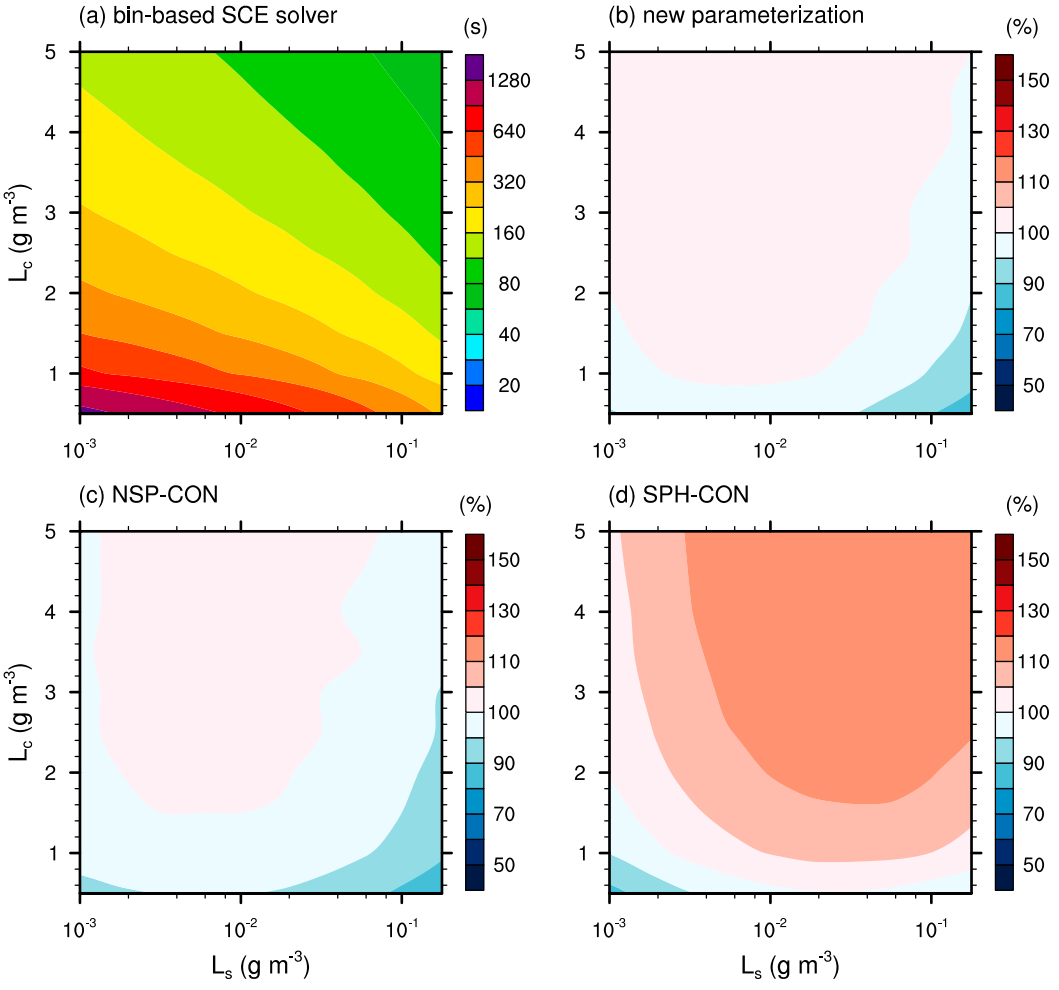

FIG. 3. Time required for 50% of the initial cloud water mass content to be converted into snow mass content via accretion t_{50} as a function of the initial cloud water mass content and the initial snow mass content obtained from (a) the bin-based solver used as the reference and percent ratios of t_{50} against the reference obtained using (b) the new parameterization, (c) NSP-CON, and (d) SPH-CON.

equation does not take into account that cloud droplets with different sizes are collected at different collection rates, the parameterizations based on this equation have been believed to yield a reasonable accuracy and thus are widely used in bulk microphysics schemes especially for the growth of raindrops, snowflakes, graupel particles, and hailstones (e.g., Wisner et al. 1972; Thompson et al. 2008; Lim and Hong 2010). In this study, two accretion parameterizations based on the continuous collection equation are derived for comparison with the new parameterization; one assumes the snowflake shape as the constant-density sphere ($\rho_s = 100\,\mathrm{kg\,m^{-3}}$), and the other employs the same nonspherical assumption for the snowflake shape as the new parameterization. These accretion parameterizations are hereafter called SPH-CON and NSP-CON, respectively. The snowflake terminal velocity and the collision efficiency for the spherical snowflake shape assumption are obtained using the same method as in section 2. The forms of the fitted functions for the spherical snowflake shape assumption are identical to those for the nonspherical snowflake shape assumption used in the new parameterization, where the values of the coefficients $v_{0,s}$, c_1, c_2, b_0, b_1, b_2, b_3, and b_4 are $202.8\,\mathrm{m^{1-c_1}\,s^{-1}}$, 0.732, $52.33\,\mathrm{m^{-1}}$, 1, $156\,222\,\mathrm{m^{-1}}$, $3.667\,\mathrm{m^{-1}}$, $2036\,\mathrm{m^{-1}}$, and $88\,340\,\mathrm{m^{-1}}$, respectively. Note that the obtained collision efficiency is used as $\overline{\eta}$ in (13), as a function of mass-weighted mean sizes of snowflakes and cloud droplets in NSP-CON and SPH-CON. The accretion parameterizations using the bulk collection efficiency may be improved if the bulk collection efficiency is expressed by a more complicated functional form or as a function of optimally weighted mean sizes, not the mass-weighted mean sizes. This improvement may deserve further research, but it is not considered in this study.

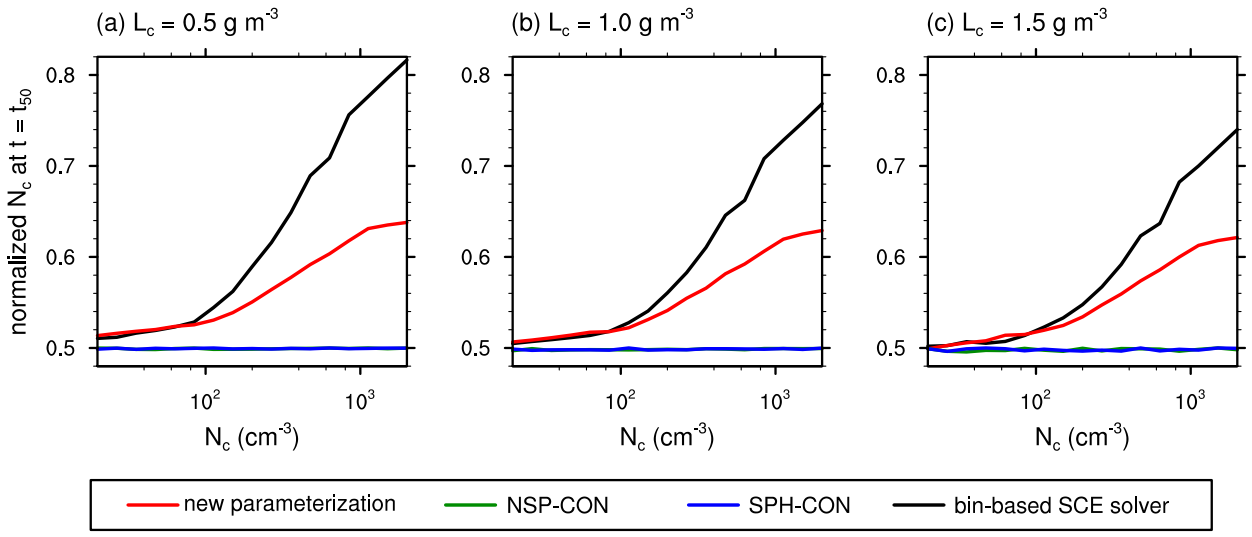

FIG. 4. Cloud droplet number concentration N_c at $t = t_{50}$ divided by its initial value as a function of the initial N_c obtained using the bin-based direct SCE solver and different accretion parameterizations. The initial cloud water mass contents are given by (a) 0.5, (b) 1.0, and (c) 1.5 g m^{-3}.

The bin-based direct SCE solver used in Lee and Baik (2017) and Jin et al. (2019) is modified and used as a reference in the box model simulations. This solver uses 147 bins for each hydrometeor species, where the mass doubles every third bin. The radius of the smallest cloud droplets considered in this solver is 0.5 μm. The snowflake shape assumption follows that of the new parameterization and NSP-CON. The initial size distributions of snowflakes and cloud droplets follow (2a) and (2b), respectively, but the size distributions evolve in time and deviate from the initial functional forms. Using the new parameterization, NSP-CON, SPH-CON, and the bin-based solver, the accretion process is simulated with various initial mass contents and number concentrations of snowflakes and cloud droplets (i.e., 0.001–0.2 g m^{-3} for the snow mass content, 0.5–5 g m^{-3} for the cloud water mass content, and 20–2000 cm^{-3} for the cloud droplet number concentration). The time step of the model integration is 1 s.

Figure 3 shows t_{50} obtained from the bin-based solver as the reference and percent ratios of t_{50} against the reference obtained using the new parameterization, NSP-CON, and SPH-CON. Here, t_{50} is the time required for 50% of the initial cloud water mass content to be converted into snow mass content through the accretion process. As the initial snow and cloud water mass contents increase, t_{50} decreases. The values of t_{50} calculated using the new parameterization and NSP-CON agree well with those calculated using the bin-based solver; the percent ratios against the reference are 87%–105% for the new parameterization and 86%–103% for NSP-CON. The deviation of t_{50} in the new parameterization and NSP-CON from that in the bin-based solver may result from the limitation of representing the evolution of the snowflake size distribution using the predefined size distribution function. SPH-CON, which has a different snowflake shape assumption from the bin-based solver, shows much larger t_{50} for a wide range of initial conditions, in other words a slower accretion process; the percent ratio against the reference is 88%–117%. This can be attributed to the smaller cross-sectional area of spherical snowflakes compared to that of nonspherical snowflakes of the same mass. When averaged over the various initial snow and cloud water mass contents, SPH-CON overestimates t_{50} by 8%, while the new parameterization overestimates t_{50} by 1% and NSP-CON underestimates t_{50} by 1%.

Both the new parameterization and the much simpler parameterization NSP-CON seem to provide good predictions for the conversion of the cloud water mass into the snow mass. However, when it comes to the change in the number concentration of cloud droplets, the new parameterization shows its superiority. Figure 4 provides the normalized N_c at $t = t_{50}$, which is the cloud droplet number concentration divided by its initial value, for different initial mass content and number concentration of cloud droplets. The normalized N_c at $t = t_{50}$ predicted by NSP-CON and SPH-CON is very close to 0.5, which means that if one-half of the cloud water mass content is consumed via the accretion process, the cloud droplet number concentration is also reduced by almost exactly 50%. The bin-based solver makes totally different predictions that the normalized N_c at $t = t_{50}$ is somewhat larger than 0.5 for all initial conditions and that it exceeds 0.8 for some initial

conditions. The prediction of the new parameterization is relatively close to that of the bin-based solver, reproducing the increases in the normalized N_c at $t = t_{50}$ with increasing N_c. As the initial cloud droplet number concentrations increase (i.e., the initial mean cloud droplet sizes decrease for a given cloud water mass content), however, the prediction of the new parameterization deviates from that of the bin-based solver.

To provide detailed explanations for these behaviors, a few examples of the evolution of cloud droplet size distribution predicted by the bin-based solver and the three accretion parameterizations are shown in Fig. 5. Here, the same initial conditions used in Fig. 4b but for three different initial cloud droplet number concentrations are used. When the initial $N_c = 100\,\mathrm{cm}^{-3}$, the cloud droplet number concentrations for different sizes predicted by the bin-based solver exhibit similar proportional decreases close to 50%, except for the leftmost and rightmost parts of the distribution (Fig. 5a). This yields the normalized N_c at $t = t_{50}$ close to 0.5. When the initial $N_c = 1000\,\mathrm{cm}^{-3}$, however, the bin-based solver predicts that the number concentrations of relatively small cloud droplets (i.e., the left part of the distribution) exhibit much smaller proportional decreases than 50% (Fig. 5b). As a compensation for this, the number concentrations of relatively large cloud droplets exhibit proportional decreases slightly greater than 50%. This yields the normalized N_c at $t = t_{50}$ far greater than 0.5. The different proportional decreases in the cloud droplet number concentrations for different sizes are induced by the inhomogeneity in the collection kernel for different cloud droplet sizes, which is mostly attributed to the inhomogeneity in the collection efficiency. Large cloud droplets are preferentially collected by snowflakes. The collection efficiency increases as the cloud droplet size increases, and its gradient is large when the cloud droplet is small and becomes small when the cloud droplet is large (Fig. 2). Therefore, the degree of inhomogeneity in the collection efficiency is low if the size distribution is mainly composed of large cloud droplets (Fig. 5a), and it is high if the size distribution is dominated by small cloud droplets (Fig. 5b). NSP-CON and SPH-CON completely fail to reproduce this behavior. The two accretion parameterizations based on the continuous collection equation predict that all cloud droplets are collected by snowflakes at the same rate. Thus, they may be suitable accretion parameterizations only for small cloud droplet number concentrations. In contrast, the new parameterization well reproduces the change in the proportional decrease of cloud droplet number concentration in virtue of using the individual particle size-dependent collection efficiency. When the initial N_c increases to $4000\,\mathrm{cm}^{-3}$, the normalized N_c at $t = t_{50}$ predicted by the bin-based solver is much higher compared to that predicted by the new parameterization (Fig. 4). This is attributed to the overestimation of collision efficiency by the fitted function for very small cloud droplets (Fig. 2c) along with the limitation of

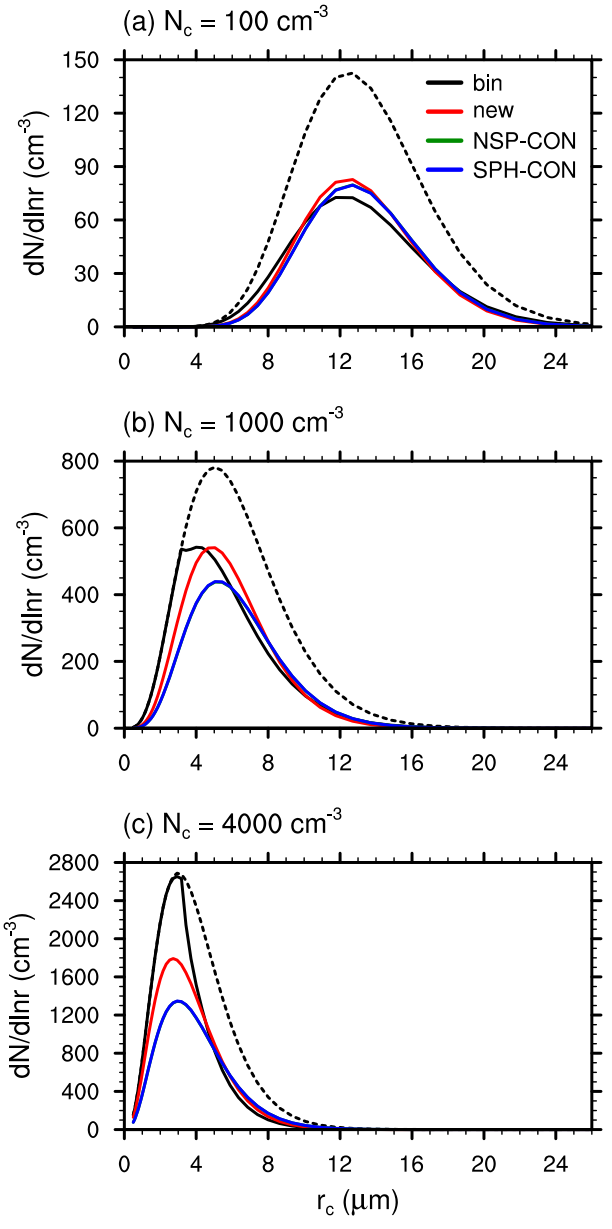

FIG. 5. Cloud droplet size distributions at the initial time (dashed line) and when $t = t_{50}$ (solid lines) in the simulations using the bin-based direct SCE solver and different accretion parameterizations. The initial mass contents of cloud water and snow are $1\,\mathrm{g\,m}^{-3}$ and $0.05\,\mathrm{g\,m}^{-3}$, respectively, and the initial number concentration of snowflakes is $2000\,\mathrm{m}^{-3}$. The initial number concentrations of cloud droplets in (a), (b), and (c) are 100, 1000, and $4000\,\mathrm{cm}^{-3}$, respectively. Note that the green lines are almost completely covered by the blue lines.

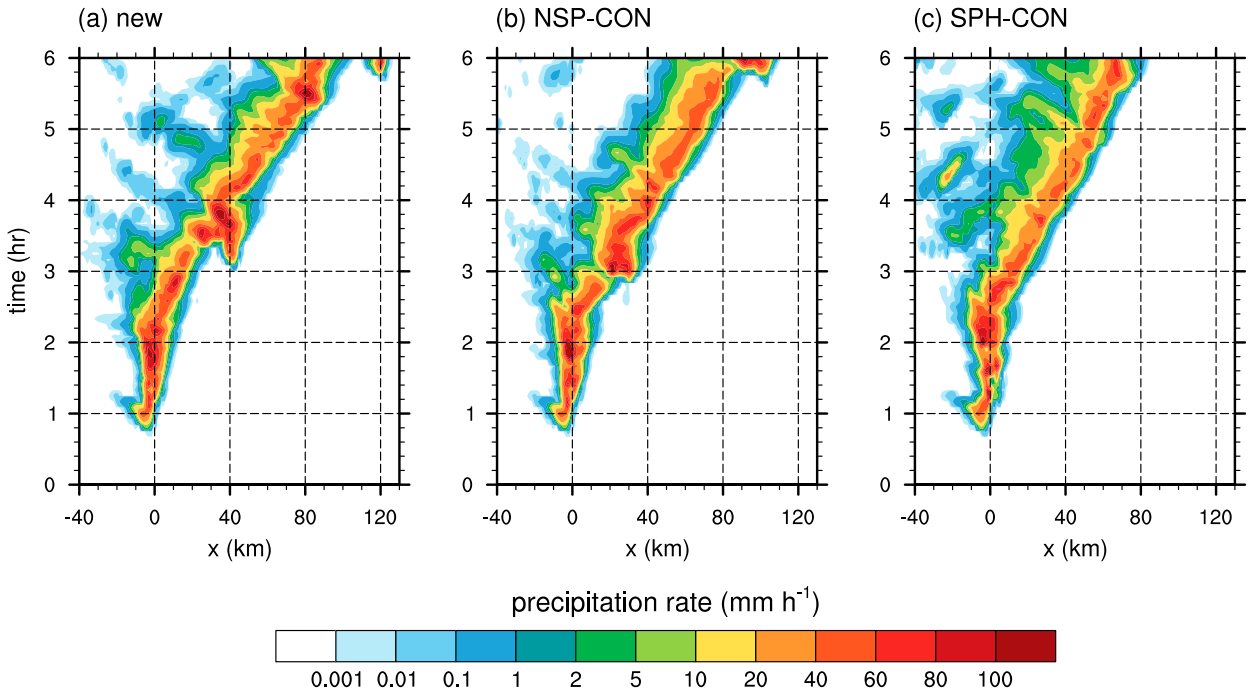

FIG. 6. Hovmöller diagrams of surface precipitation rates obtained using (a) the new parameterization, (b) NSP-CON, and (c) SPH-CON.

representing the evolution of the cloud droplet size distribution using the predefined size distribution function. Nonetheless, the new parameterization still gives results that are much closer to that of the bin-based solver compared to the other accretion parameterizations.

4. Cloud-resolving model results

a. Idealized simulations

As shown in the previous section, the new parameterization shows a relatively good performance in predicting the mass and number conversion of cloud droplets compared to the other accretion parameterizations; however, whether this better performance of the new parameterization actually leads to significant changes in cloud and precipitation simulations remains to be investigated. For the cloud-resolving simulations, the new accretion parameterization is implemented in the Weather Research and Forecasting (WRF) Model, v.4.0.3 (Skamarock et al. 2008). The parameterization of the accretion of cloud water by snow in the WRF double-moment 6-class (WDM6) microphysics scheme (Lim and Hong 2010) is replaced by the new parameterization, as well as by NSP-CON and SPH-CON. The parameterizations of all the other microphysical processes in the WDM6 scheme remain unchanged.

An idealized 2D squall-line case similar to the test case introduced in the WRF Model is simulated using the different accretion parameterizations. A squall line is a linear mesoscale convective system (MCS) characterized by a convective core region with heavy precipitation and a trailing stratiform region with relatively light precipitation. Because of a wide variety of microphysical and dynamical processes in squall lines and their sensitivities to changes in model physics, squall lines have been often used for testing a new development in numerical models (e.g., Lim and Hong 2010; Milbrandt and Morrison 2016; Morrison et al. 2016; Jensen et al. 2018). The horizontally homogeneous initial thermodynamic sounding is adopted from Weisman and Klemp (1982) with the water vapor mixing ratio near the surface set to $14\,g\,kg^{-1}$. The low-level vertical shear of the horizontal wind is initially set to $0.0048\,s^{-1}$ from the surface to $z = 2.5$ km. The initial horizontal wind speed becomes zero at $z = 2.5$ km, and it remains zero above it. As in Morrison et al. (2016), the horizontal domain size is 500 km with a constant grid spacing of 1 km, and the vertical domain size is 20 km with 80 layers using a grid spacing stretched from 225 to 290 m. An open boundary condition is applied at lateral boundaries. A sponge layer is located in the top 5 km of the domain. The time step is 5 s, and the model is integrated for 6 h. An axially symmetric initial thermal perturbation (warm bubble) is applied to initiate convection.

Figure 6 shows the Hovmöller diagrams of surface precipitation rates obtained using the different accretion parameterizations. The surface precipitation is initiated at $t \sim 40$ min, and the region of the heaviest precipitation

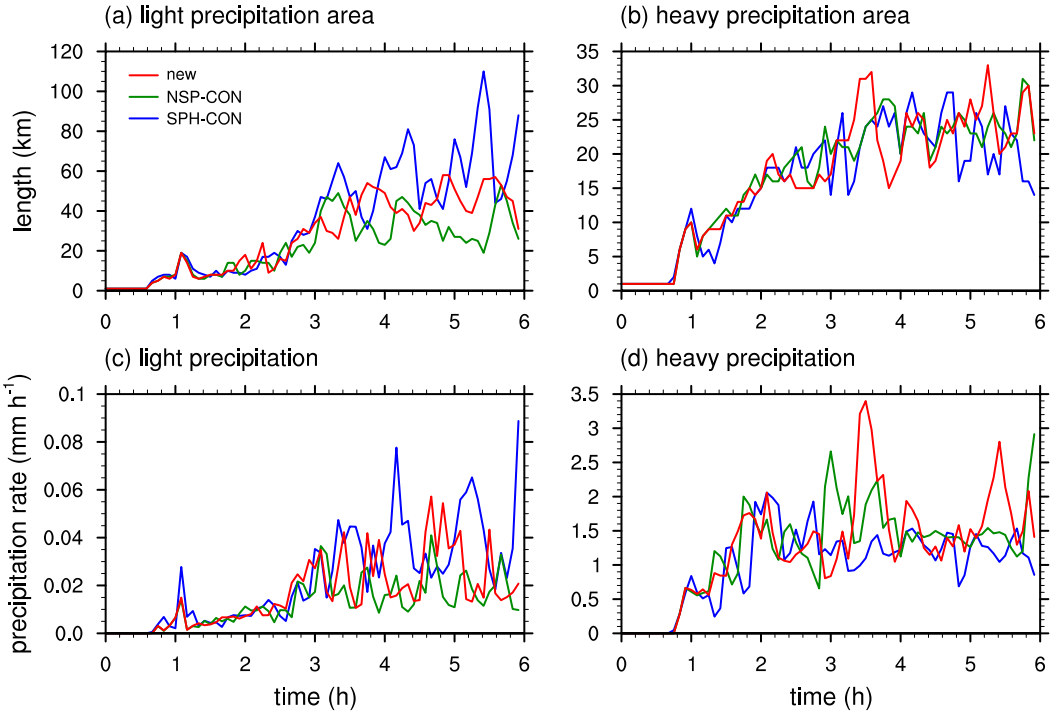

FIG. 7. Time series of areas with (a) light (10^{-3}–2 mm h^{-1}) and (b) heavy precipitation (>10 mm h^{-1}) rates. The length on the y axis in (a) and (b) indicates the total number of the model grid cells with light or heavy precipitation rates multiplied by the model grid spacing. Time series of domain-averaged precipitation rates for the (c) light and (d) heavy precipitation.

starts to move eastward after $t \sim 2$ h in all simulations. Then, the stratiform region with relatively light precipitation trails behind the eastward-moving convective core region with heavy precipitation, forming a typical structure of leading line-trailing stratiform squall lines. The squall lines simulated using the different accretion parameterizations show different precipitation intensities, precipitation distributions, and propagation speeds from each other. The new parameterization and NSP-CON predict somewhat intense precipitation in the convective core region than SPH-CON. In addition, the speed of the leading edge is slowest in SPH-CON; the leading edge at $t = 5$ h in SPH-CON is ~15 km behind that in the new parameterization and NSP-CON. Compared to NSP-CON, the new parameterization predicts a broader area of the trailing stratiform precipitation. Even at $t = 5$–6 h when the leading edge reaches $x \sim 100$ km, a considerable area of light precipitation still remains $x < 40$ km in the new parameterization.

Figure 7 shows the time series of areas with light (10^{-3}–2 mm h^{-1}) and heavy (>10 mm h^{-1}) precipitation rates and domain-averaged surface precipitation rates for these light and heavy precipitation. NSP-CON predicts the smallest area of light precipitation among the accretion parameterizations, 19% and 37% smaller on average compared to the new parameterization and SPH-CON, respectively. Similarly, the domain-averaged light precipitation rate is smallest in NSP-CON, 24% and 45% smaller on average compared to the new parameterization and SPH-CON, respectively. The domain-averaged heavy precipitation rates predicted by the new parameterization and NSP-CON are similar to each other, and are 24% and 20% greater on average, respectively, in comparison with SPH-CON. There are no significant differences in the area of heavy precipitation between the accretion parameterizations.

Figure 8 shows the probability density functions (PDFs) of the logarithm of surface precipitation rates. For almost all precipitation rates smaller than ~2 mm h^{-1}, the new parameterization shows higher frequencies than NSP-CON. In contrast, the new parameterization tends to have lower frequencies of precipitation rates greater than ~2 mm h^{-1}. These opposite tendencies for light and heavy precipitation rates can be attributed to the different microphysical conditions created by the new parameterization and NSP-CON, as will be explained later. As can be also found in Fig. 6, SPH-CON predicts much lower frequencies of precipitation rates greater than ~10 mm h^{-1} and higher frequencies of precipitation rates between ~1 and ~10 mm h^{-1} compared to the

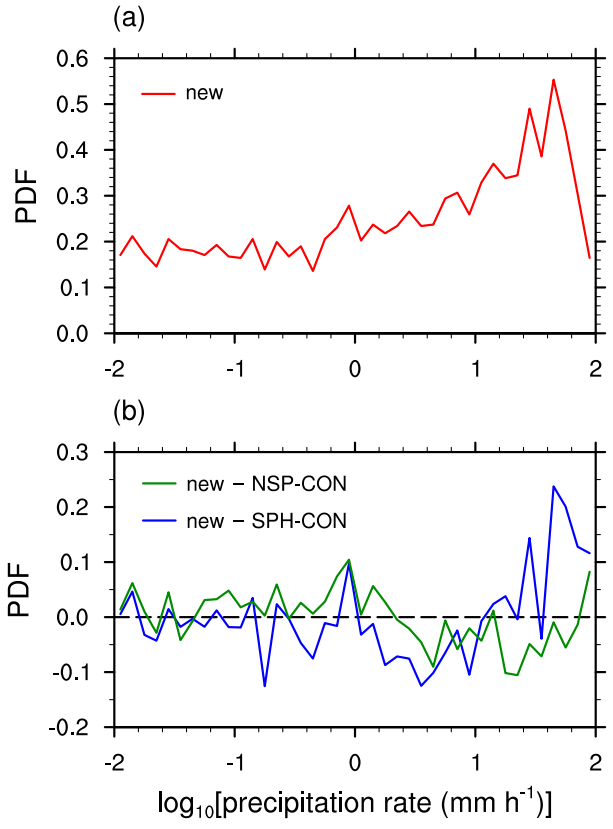

FIG. 8. (a) Probability density function (PDF) for the logarithm of precipitation rate obtained using the new parameterization and (b) differences in PDFs between the new parameterization and the two other accretion parameterizations, NSP-CON and SPH-CON. The black dashed line in (b) represents zero values of the PDF differences.

new parameterization. For precipitation rates smaller than ~1 mm h^{-1}, no consistent positive or negative difference in frequency between the new parameterization and SPH-CON is found.

It is noted that the differences in precipitation properties between the accretion parameterizations shown in Figs. 7 and 8 contain some randomness. Ensemble simulations with perturbations in the initial potential temperature fields are additionally conducted to check this point. The differences in precipitation properties between the accretion parameterizations in the majority of the ensemble sets are qualitatively similar to those in the simulations with unperturbed initial condition. However, the degree of the differences between the ensemble means with different accretion parameterizations is largely reduced for the properties investigated in Figs. 7 and 8, and the differences in the PDFs of precipitation rates between the new parameterization and NSP-CON deviates from those in the unperturbed simulations for a certain range of precipitation rate (not shown).

The different microphysical properties caused by the different accretion parameterizations are examined. Figure 9 shows the horizontally averaged vertical profiles of microphysical variables that are closely related to the accretion process such as the snow mixing ratio, the accretion rate, the mass-weighted mean cloud droplet radius, and the vertical mass flux of cloud water, averaged over t = 2–6 h when the typical structure of the squall line is present. In the new parameterization, snow exists above $z \sim 3.3$ km, and the accretion process takes place in $z \sim 3.5$–9.8 km where snow and cloud water coexist (Figs. 9a,b). The maximum accretion rate appears at $z \sim 5.5$ km, and the maximum snow mixing ratio appears ~1.8 km above that level. The upward mass flux of cloud water driven by in-cloud updrafts exhibits its maximum at $z \sim 4$ km, providing cloud droplets to the upper level (Fig. 9d).

As the cloud droplets enter the level where the accretion process occurs, they start to be collected by snowflakes. As mentioned in the previous section, large cloud droplets are preferentially collected by snowflakes in the new parameterization, resulting in a fast decrease in the mean radius of cloud droplets compared to NSP-CON where this feature is not considered. This smaller mean radius of cloud droplets is seen in $z \sim 2.5$–5 km in Fig. 9g. Because of the smaller mean size of cloud droplets in the new parameterization, the accretion rate becomes smaller ($z \sim 4$–5 km), and the upward transport of cloud droplets that are not collected by snowflakes becomes larger (Figs. 9f,h). The greater vertical mass flux of cloud water increases the cloud water mass in the relatively upper level, and thus, the accretion rate in the new parameterization eventually becomes larger in $z \sim$ 5.3–9.5 km compared to NSP-CON. As a result, the snow mixing ratio at upper levels ($z \sim 5.8$–10.3 km) is greater in the new parameterization (Fig. 9e). Snowflakes at upper levels remain aloft for longer times than snowflakes at relatively lower levels, during which the snowflakes descend rearward relative to the storm motion. Because the melting of the snowflakes falling to the rear part of the squall line is responsible for the trailing stratiform precipitation, the larger amount of upper-level snow in the new parameterization results in the broadening of the area of the trailing stratiform precipitation, and the enhancement of the precipitation in that area, as found in Figs. 7 and 8. SPH-CON inherently predicts weaker accretion process than the other parameterizations (Fig. 3). The accretion rate at upper levels ($z \sim$ 6.5–10 km) in SPH-CON is even smaller than that in NSP-CON, which may lead to a reduction in latent heat release and a consequent reduction in the updraft velocity at upper levels. The smaller upward transport of cloud water at upper levels in SPH-CON compared to NSP-CON is

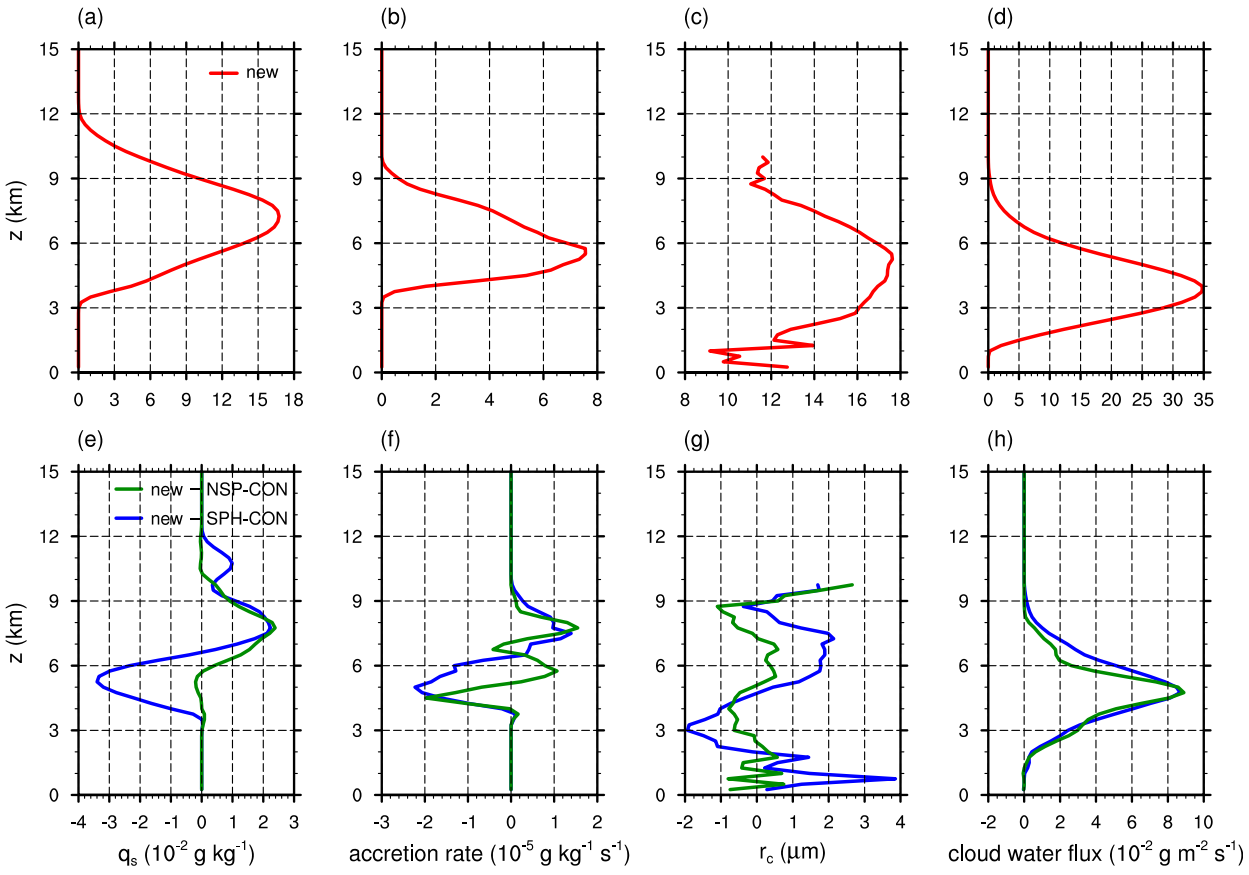

FIG. 9. Domain-averaged vertical profiles of (a) snow mixing ratio, (b) rate of accretion of cloud water by snow, (c) mass-weighted mean cloud droplet radius, and (d) vertical mass flux of cloud water obtained using the new parameterization, and (e)–(h) their differences between the new parameterization and the two other accretion parameterizations, NSP-CON and SPH-CON.

found in Fig. 9h. As a result, snow is distributed to relatively lower levels in SPH-CON compared to the new parameterization and NSP-CON (Fig. 9e).

Differences resulting from the different shape assumptions for snowflakes are prominent in the thermodynamic and dynamic fields. Figure 10 shows the temporal evolution of the intensity and areal fraction of the cold pool obtained using the perturbation potential temperature θ' at the lowest model level. SPH-CON tends to predict the warmest cold pool and the slowest expansion of the cold pool among the accretion parameterizations. The different cold pool intensities and expansion speeds predicted by the different accretion parameterizations could result in differences in the dynamics such as low-level convergence and convective strength, although this effect can vary with circumstances.

b. *Real-case simulations*

In the idealized squall-line simulations described above, the preferential collection of large cloud droplets and the relatively realistic shape of snowflakes considered in the new parameterization lead to nonnegligible changes in the distributions of precipitation and in the microphysical and dynamical properties of the storm. For further evaluation, a real precipitation event that was influenced by more complex environment than the idealized environment is simulated using the different accretion parameterizations. The precipitation event occurred on 26 July 2019 over the Korean Peninsula. A linear MCS elongated in the southwest–northeast direction formed over North Korea around 0000 LST 26 July by the changma front, a quasi-stationary front separating the warm and moist air mass in the south side and the relatively cold air mass in the north side during the East Asian summer monsoon period. The system moved southward and slowly passed over the central Korean Peninsula within ~15 h. At lower levels, southwesterly winds continuously transported a large amount of moisture to the system, and westerly winds were dominant at upper levels. According to the automatic weather station (AWS) observations operated by the Korea Meteorological

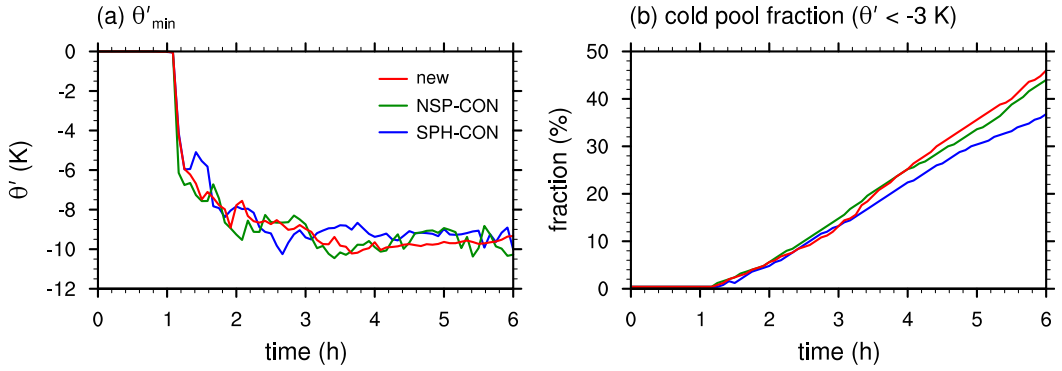

FIG. 10. Time series of (a) minimum θ' at the lowest model level ($z \sim 140$ m) and (b) fraction of domain area covered by the lowest-level cold pool defined by the −3-K θ' isotherm. Only the right half of the domain is used for calculation.

Administration (KMA), the maximum 12-h accumulated surface precipitation amount from 0300 to 1500 LST 26 July reached ~150 mm at a station in the mountainous region close to the east coast (38.33°N, 128.31°E).

Figure 11 shows the configuration of the model domain. Three one-way nested domains that have horizontal grid spacings of 27, 9, and 3 km, respectively, are used. The numbers of horizontal grids for domains 1, 2, and 3 are 150 × 120, 217 × 184, and 253 × 244, respectively. Vertically 42 layers with the grid spacing being stretched from ~60 m in the lowest layer to ~600 m in the highest layer are considered for all three domains. The height of the domain top is ~20 km (50 hPa). The physics parameterizations used for the WRF Model simulations are the same as those used in Jin et al. (2019) except for the microphysics scheme; the Kain–Fritsch cumulus parameterization scheme (Kain 2004), the Yonsei University (YSU) planetary boundary layer scheme (Hong et al. 2006), the Dudhia shortwave radiation scheme (Dudhia 1989), the Rapid Radiative Transfer Model (RRTM) longwave radiation scheme (Mlawer et al. 1997), the unified Noah land surface model (Tewari et al. 2004), and the MM5 similarity surface-layer scheme (Zhang and Anthes 1982). The cumulus parameterization scheme is turned off in the innermost domain. The model is integrated for 18 h starting from 2100 LST 25 July 2019, and the simulation data of the last 12 h in a selected domain where the system was mainly located during those 12 h (yellow box in Fig. 11) are used for analysis in this study. The boundary conditions for the outermost domain and the initial conditions are obtained from National Centers for Environmental Prediction (NCEP) final analysis data (NCEP 2015) that have a time interval of 6 h and a horizontal resolution of 0.25°. The synoptic patterns are well reproduced by the simulations using the new parameterization, NSP-CON, and SPH-CON (not shown).

To evaluate the accuracy of the simulations, the Brier score is calculated by comparing the predicted 12-h accumulated surface precipitation amount at each AWS point with the observed value. Surface precipitation data from 271 AWSs located inside the yellow box in Fig. 11 are used. The Brier scores are shown in Fig. 12. A low Brier score corresponds to a better accuracy of precipitation prediction. The new parameterization gives lower Brier scores for almost all thresholds greater than 28 mm compared to SPH-CON. Compared to NSP-CON, the new parameterization gives lower Brier scores for almost all thresholds of 21–87 mm. However, it seems that the improvement of the model performance on precipitation prediction achieved by the use of a more sophisticated

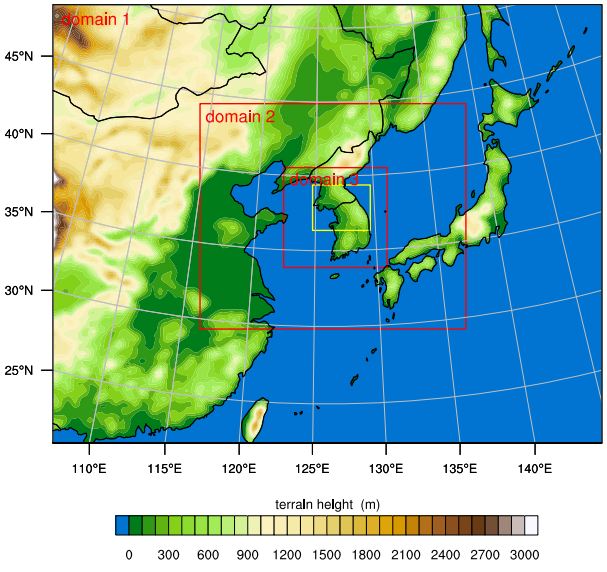

FIG. 11. Domain configuration for the real-case simulations and topography. Domains 1, 2, and 3 correspond to the three nested model domains, and the yellow box corresponds to the analysis domain.

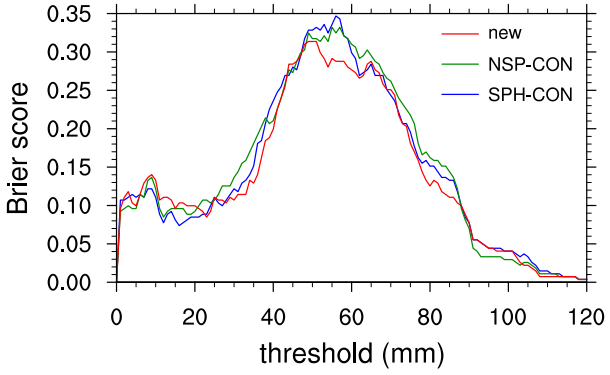

FIG. 12. Brier scores calculated comparing the predicted 12-h accumulated surface precipitation amount at each AWS point with the observed value.

parameterization for the snowflake–cloud droplet accretion process is not dramatic.

The Hovmöller diagrams of zonally averaged surface precipitation rates obtained using the different accretion parameterizations are examined (Fig. 13). During this precipitation event, the changma front moves southward, so the precipitation system follows its southward movement. The individual convective cells, however, are advected northeastward by the southwesterly winds at lower levels or eastward by the westerly winds at upper levels. The heaviest precipitation (reddish area in Fig. 13) is found in ~38.4°–38.7°N during ~0300–0500 LST in all simulations. In this region and time period, the new parameterization predicts larger precipitation rates compared to SPH-CON. Compared to NSP-CON, the new parameterization shows smaller precipitation rates in the heavy precipitated region in the period ~0600–0900 LST. Some differences in the areas of light precipitation (bluish area in Fig. 13) are also found in the period ~1000–1200 LST, but it is difficult to conduct a quantitative comparison from this figure.

The PDFs of surface precipitation rates are shown in Fig. 14. Although the magnitudes of the differences in the PDFs are relatively small compared to those that appeared in the idealized simulations (Fig. 8b) possibly due to more complicated conditions in the real environment, the important features in Fig. 8b are also found in Fig. 14b. The new parameterization tends to show higher frequencies of precipitation rates smaller than $1\,\mathrm{mm\,h^{-1}}$ and lower frequencies of precipitation rates greater than $3\,\mathrm{mm\,h^{-1}}$ compared to NSP-CON. SPH-CON tends to predict lower frequencies of precipitation rates greater than $10\,\mathrm{mm\,h^{-1}}$ and higher frequencies of precipitation rates between 0.2 and $10\,\mathrm{mm\,h^{-1}}$. This suggests that the differences in the accretion parameterizations make consistent changes in the distributions of precipitation also in the simulations of a real precipitation event. Note that the effects of the new parameterization on precipitation properties in the real-case simulations may contain some randomness as in the

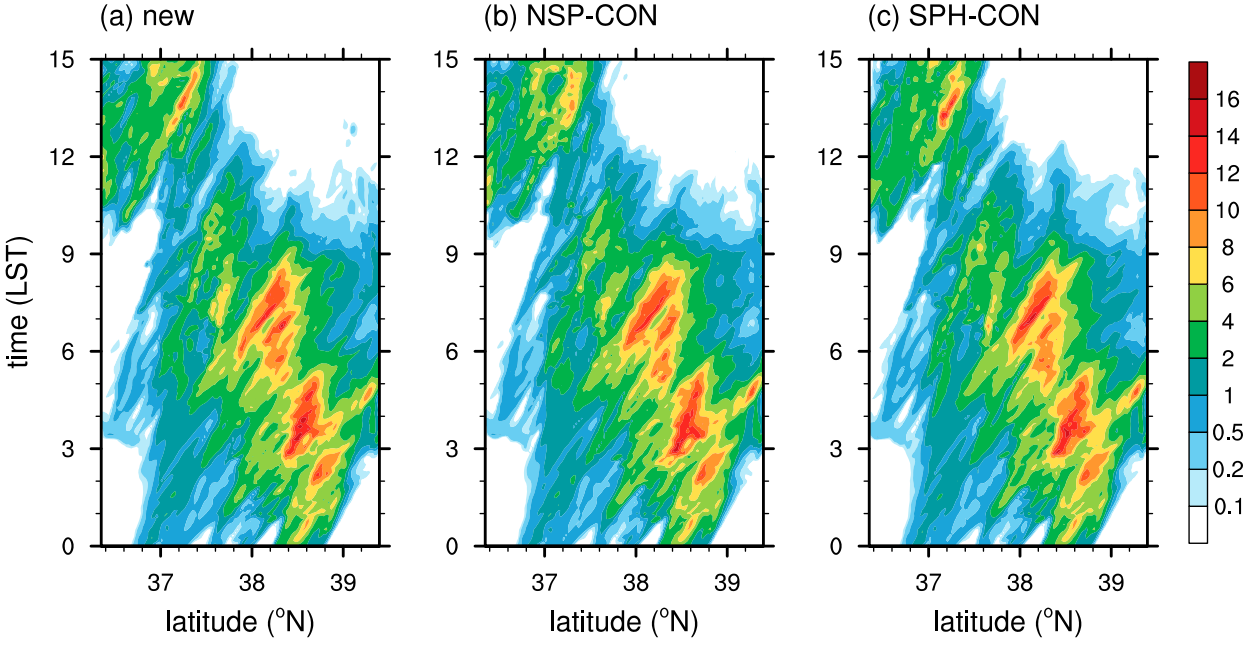

FIG. 13. Hovmöller diagrams of zonally averaged surface precipitation rates ($\mathrm{mm\,h^{-1}}$) obtained using (a) the new parameterization, (b) NSP-CON, and (c) SPH-CON.

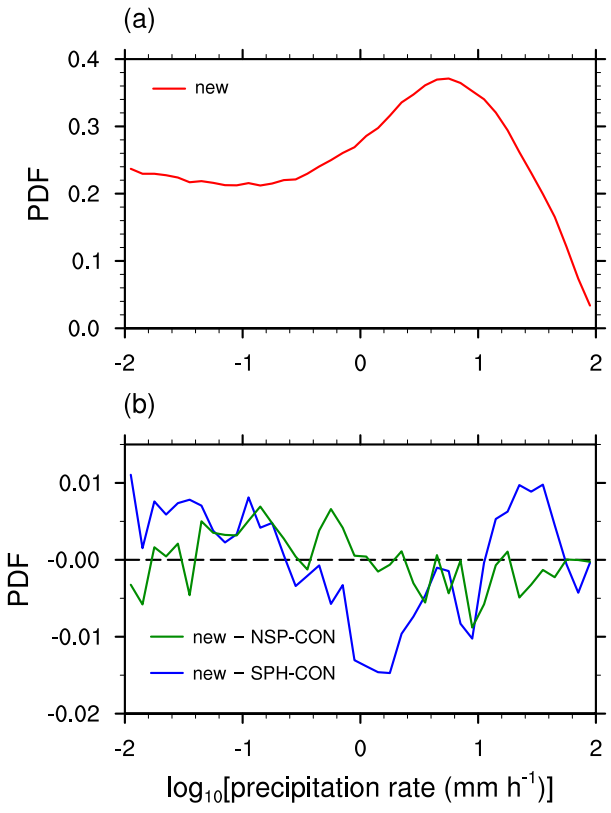

FIG. 14. As in Fig. 8, but for the real-case simulations.

idealized simulations. Ensemble simulations with slightly different realizations of this case may reduce the problem, but they are not tried in this study.

Figure 15 shows the horizontally averaged vertical profiles of the snow mixing ratio, the accretion rate, the depletion rate of cloud droplet number concentration via the accretion process, the mass-weighted mean cloud droplet radius, and the vertical mass flux of cloud water, averaged from 0300 to 0900 LST when the precipitation is most intense (see Fig. 13). Because of the higher freezing level compared to that in the idealized simulations, the accretion process takes place at relatively higher altitudes; snow is present in $z \sim 4$–14.5 km, and the accretion process occurs in $z \sim 4.5$–11 km with the maximum accretion rate at $z \sim 6$ km in the new parameterization (Figs. 15a,b). Compared to NSP-CON, the new parameterization predicts smaller cloud droplet number depletion rate that reflects the preferential collection of large cloud droplets by snowflakes in the new parameterization (Figs. 15c,h). This results in the smaller mean cloud droplet size in the new parameterization (Figs. 15d,i). The smaller accretion rate in $z \sim 4.5$–7.8 km in the new parameterization is attributed to the smaller mean size of cloud droplets (Fig. 15g). The upper-level accretion rate in the new parameterization was expected to be larger compared to the other accretion parameterizations as in Fig. 9g. The new parameterization does predict the larger accretion rate in $z \sim 8$–11.8 km, but the difference is not so large despite the larger upward transport of cloud droplets (Figs. 15e,j). One possible reason for this is the strong advection of snow at upper levels. Unlike the idealized simulations where no basic wind is present at upper levels, the real-case simulations have strong westerly winds at upper levels. Snow produced at upper levels does not stay around its original location for a long time and spreads horizontally to the region where supplies of cloud water from lower levels are relatively insufficient. As a result, the upper-level accretion rate in the new parameterization is only slightly larger compared to the other parameterizations, while the snow mixing ratio is significantly larger in $z \sim 9.3$–15 km (Fig. 15f). The widespread upper-level snowflakes grow by microphysical processes other than the accretion of cloud droplets, such as deposition process (not shown).

Figure 16 shows the time-averaged horizontal distributions of the snow water path, the column-integrated snow mass content. The area with a snow water path greater than 1 kg m^{-2} in the new parameterization is 7% broader compared to that in NSP-CON, while these two accretion parameterizations predict almost the same amount of total snow mass in the domain area. The widespread snow eventually falls to the melting layer and makes a contribution to producing the stratiform precipitation, so its difference can affect the frequencies of light precipitation rates shown in Fig. 14. The higher frequencies of light precipitation rates in the new parameterization compared to NSP-CON seems to be related to this feature. The horizontally broader distribution of snow in the new parameterization compared to NSP-CON along with the upper distribution of snow (Fig. 15f) may affect the thermodynamic fields via the consequent changes in latent heating and radiation.

Because the smaller mean cloud droplet size in the new parameterization induced by the smaller cloud droplet number depletion rate may have some effects on the radiative properties of the simulated clouds, the optical thickness of cloud droplets is also examined. Among the accretion parameterization, the new parameterization predicts the greatest optical thickness of cloud droplets on average as expected, but the differences are small in the simulations of this particular case (not shown).

Compared to the 2D idealized simulations in the previous section, the differences between the real-case simulation results obtained using the different accretion parameterizations are less pronounced. The magnitudes of the differences shown in Figs. 14 and 15 are much

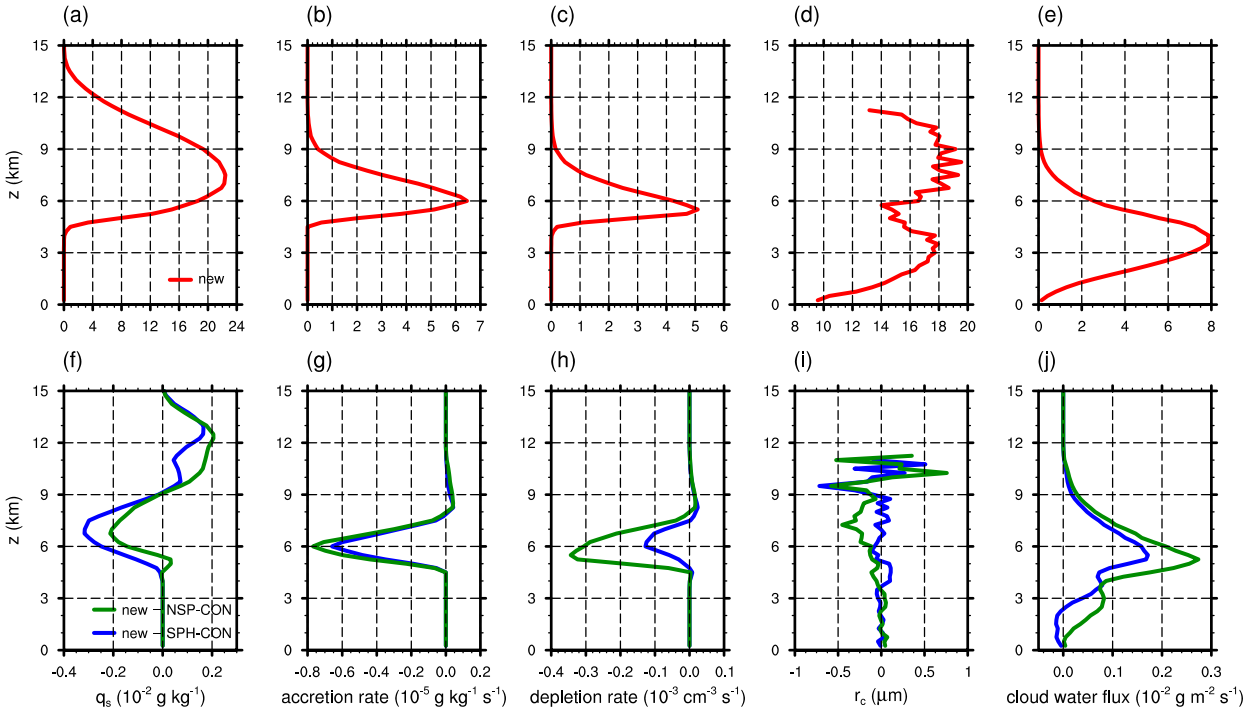

FIG. 15. Domain-averaged vertical profiles of (a) snow mixing ratio, (b) rate of accretion of cloud water by snow, (c) rate of depletion of cloud droplet number concentration via the accretion process, (d) mass-weighted mean cloud droplet radius, and (e) vertical mass flux of cloud water obtained using the new parameterization, and (f)–(j) their differences between the new parameterization and the two other accretion parameterizations, NSP-CON and SPH-CON.

smaller than those in Figs. 8 and 9. In the real-case simulations, the environmental conditions are more complicated, and various physical processes that are ignored in the idealized simulations are considered. As the vertical profiles of the accretion rate are affected by strong upper-level winds (Fig. 15g), the complexity of the real environment may modify the effects of the newly developed parameterization in various directions. The analysis on dynamics was also performed for the real-case simulation results, but the magnitudes of the differences between the results obtained from the different accretion parameterizations were found to be very small although the differences were qualitatively similar to those found in the idealized simulations (not shown). In the idealized simulations, the cold pool directly related to the microphysical processes is a main factor for the low-level convergence that maintains the system. In the real-case simulations in this study, however, the low-level convergence that maintains the MCS is mainly provided by the changma front created by a synoptic-scale forcing. This could be one reason that the implementation of the different accretion parameterizations does not affect the dynamical features in the simulations significantly. The cases in which the simulation of clouds and precipitation is crucially affected by the choice of the accretion parameterization will be examined in future studies.

5. Summary and conclusions

A new parameterization of the accretion of cloud water by snow for use in bulk microphysics schemes is derived as an analytic approximation of the SCE. For this parameterization, a fitted function of collection efficiency of individual snowflake–cloud droplet pairs is obtained by employing Böhm's collision efficiency. Using a box model, the performance of the new parameterization is evaluated by comparing it with the bin-based direct SCE solver and two other accretion parameterizations. The two accretion parameterizations that are both based on the continuous collection equation but have different assumptions for the snowflake shape, NSP-CON and SPH-CON, are also compared with the new parameterization. The time required for the mass conversion from cloud water to snow via the accretion process is well predicted by the new parameterization and NSP-CON, while SPH-CON overestimates this time attributable to the smaller cross-sectional area of spherical snowflakes compared to that of nonspherical snowflakes of the same mass.

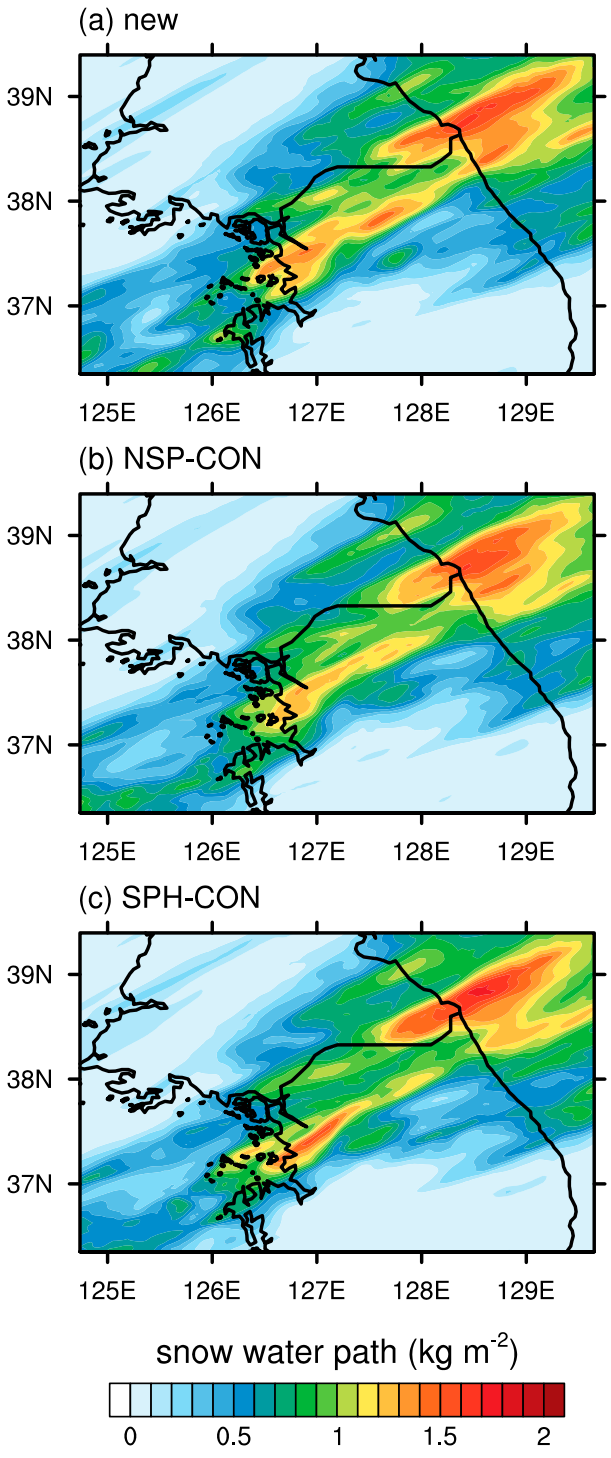

FIG. 16. Time-averaged horizontal distributions of snow water path obtained using (a) the new parameterization, (b) NSP-CON, and (c) SPH-CON.

The new parameterization shows its superiority over the other accretion parameterizations in the prediction of the number conversion via the accretion process. Only the new parameterization among the accretion parameterizations predicts the slower proportional decrease in the cloud droplet number concentration compared to that in the cloud water mass, which is also predicted by the bin-based solver. This suggests that the new parameterization based on the SCE successfully reflects the preferential collection of large cloud droplets by snowflakes that stems from the individual particle size-dependent collection efficiency.

The different characteristics of the accretion parameterizations found in the box model simulations induce significant differences in the simulations of cloud and precipitation. Using the WRF Model where the new parameterization as well as the other parameterizations are implemented, an idealized squall line is simulated. The new parameterization predicts a larger area of light precipitation, a greater domain-averaged precipitation rate of light precipitation, and higher frequencies of light precipitation rates compared to NSP-CON. The fast decrease in the mean cloud droplet size in the new parameterization reduces the accretion rate at relatively lower levels and increases the accretion rate at relatively upper levels. The resultant increase in the upper-level snow mixing ratio leads to the broadening of the area of the trailing stratiform precipitation. SPH-CON predicts the weaker convective activity in the convective core, which results in a smaller domain-averaged heavy precipitation rate and a lower frequency of heavy precipitation compared to the other parameterizations.

A heavy precipitation event with a linear MCS that passed over the central Korean Peninsula is simulated to evaluate the effects of the new parameterization in real-case simulations. In this particular case, the simulation with the new parameterization yields the best prediction of accumulated precipitation compared to those with the other accretion parameterizations, although more rigorous evaluation through multiple realizations of this case may be needed for robustness of this result. The differences in the precipitation prediction between the simulations seem to be much smaller than the overall errors of the model prediction from the observation. As in the idealized simulations, the new parameterization tends to show higher frequencies of light precipitation rates and lower frequencies of heavy precipitation rates. The relatively large amount of upper-level snow in the new parameterization is again found in the real-case simulations, and it affects the area with the snow water path exceeding a threshold, which may be related to the higher frequencies of light precipitation rates.

Although the degree of the effects of the new parameterization on the simulations of clouds and precipitation may depend on the environmental conditions of precipitation events, the new parameterization predicts qualitatively different microphysical structures of

the precipitating system and different characteristics of precipitation from those predicted by the other accretion parameterizations. This implies that the new parameterization based on a better physical representation of the accretion process in reality should be employed to better predict clouds and precipitation in some cases where the choice of the accretion parameterization is important. Especially, because double-moment microphysics schemes are being introduced into weather and climate models, the better prediction of the cloud droplet number concentration in the new parameterization can give some advantages to the models. Additionally, the development of more elaborate parameterizations of other collection processes that are currently treated in a relatively simple way is encouraged, and this will be studied in a future work. The usefulness of the new approach in the collection parameterizations can be further investigated by comparing the sensitivity of the simulations to the different approaches in the collection parameterizations with the sensitivities to other uncertainties in the model such as initial conditions and uncertain microphysical parameters.

The new parameterization is developed for use in conventional bulk microphysics schemes, but it can be modified to be applied in some of the new microphysics models that prognose ice particle properties. For this, the coefficients in the collection efficiency function should be parameterized as functions of the ice particle properties, which may be done in a future work.

Acknowledgments. The authors are grateful to three anonymous reviewers whose valuable comments helped improve this paper. This work was supported by the Research Institute of Basic Sciences funded by the National Research Foundation of Korea (NRF-2019R1A6A1A10073437) and also supported by the Korea Meteorological Administration Research and Development Program under Grant KMI 2020-00710.

REFERENCES

Baldauf, M., A. Seifert, J. Förstner, D. Majewski, M. Raschendorfer, and T. Reinhardt, 2011: Operational convective-scale numerical weather prediction with the COSMO model: Description and sensitivities. *Mon. Wea. Rev.*, **139**, 3887–3905, https://doi.org/10.1175/MWR-D-10-05013.1.

Beard, K. V., 1976: Terminal velocity and shape of cloud and precipitation drops aloft. *J. Atmos. Sci.*, **33**, 851–864, https://doi.org/10.1175/1520-0469(1976)033<0851:TVASOC>2.0.CO;2.

Böhm, H. P., 1989: A general equation for terminal fall speed of solid hydrometeors. *J. Atmos. Sci.*, **46**, 2419–2427, https://doi.org/10.1175/1520-0469(1989)046<2419:AGEFTT>2.0.CO;2.

——, 1994: Theoretical collision efficiencies for riming and aerosol impaction. *Atmos. Res.*, **32**, 171–187, https://doi.org/10.1016/0169-8095(94)90058-2.

——, 1999: Revision and clarification of "A general hydrodynamic theory for mixed-phase microphysics." *Atmos. Res.*, **52**, 167–176, https://doi.org/10.1016/S0169-8095(99)00033-2.

Brandes, E. A., K. Ikeda, G. Zhang, M. Schonhuber, and R. M. Rasmussen, 2007: A statistical and physical description of hydrometeor distributions in Colorado snowstorms using a video disdrometer. *J. Appl. Meteor. Climatol.*, **46**, 634–650, https://doi.org/10.1175/JAM2489.1.

Brdar, S., and A. Seifert, 2018: McSnow: A Monte-Carlo particle model for riming and aggregation of ice particles in a multidimensional microphysical phase space. *J. Adv. Model. Earth Syst.*, **10**, 187–206, https://doi.org/10.1002/2017MS001167.

Connolly, P. J., C. Emersic, and P. R. Field, 2012: A laboratory investigation into the aggregation efficiency of small ice crystals. *Atmos. Chem. Phys.*, **12**, 2055–2076, https://doi.org/10.5194/acp-12-2055-2012.

Dudhia, J., 1989: Numerical study of convection observed during the Winter Monsoon Experiment using a mesoscale two-dimensional model. *J. Atmos. Sci.*, **46**, 3077–3107, https://doi.org/10.1175/1520-0469(1989)046<3077:NSOCOD>2.0.CO;2.

Field, P. R., R. J. Hogan, P. R. A. Brown, A. J. Illingworth, T. W. Choularton, and R. J. Cotton, 2005: Parameterization of ice-particle size distributions for mid-latitude stratiform cloud. *Quart. J. Roy. Meteor. Soc.*, **131**, 1997–2017, https://doi.org/10.1256/qj.04.134.

Gaudet, B. J., and J. M. Schmidt, 2005: Assessment of hydrometeor collection rates from exact and approximate equations. Part I: A new approximate scheme. *J. Atmos. Sci.*, **62**, 143–159, https://doi.org/10.1175/JAS-3362.1.

Heymsfield, A. J., 2003: Properties of tropical and midlatitude ice cloud particle ensembles. Part I: Median mass diameters and terminal velocities. *J. Atmos. Sci.*, **60**, 2573–2591, https://doi.org/10.1175/1520-0469(2003)060<2573:POTAMI>2.0.CO;2.

——, A. Bansemer, C. Schmitt, C. Twohy, and M. R. Poellot, 2004: Effective ice particle densities derived from aircraft data. *J. Atmos. Sci.*, **61**, 982–1003, https://doi.org/10.1175/1520-0469(2004)061<0982:EIPDDF>2.0.CO;2.

Hong, S.-Y., and J.-O. J. Lim, 2006: The WRF single-moment 6-class microphysics scheme (WSM6). *J. Korean Meteor. Soc.*, **42**, 129–151.

——, Y. Noh, and J. Dudhia, 2006: A new vertical diffusion package with an explicit treatment of entrainment processes. *Mon. Wea. Rev.*, **134**, 2318–2341, https://doi.org/10.1175/MWR3199.1.

Houze, R. A., Jr., P. V. Hobbs, P. H. Herzegh, and D. B. Parsons, 1979: Size distributions of precipitation particles in frontal clouds. *J. Atmos. Sci.*, **36**, 156–162, https://doi.org/10.1175/1520-0469(1979)036<0156:SDOPPI>2.0.CO;2.

Jensen, A. A., J. Y. Harrington, H. Morrison, and J. A. Milbrant, 2017: Predicting ice shape evolution in a bulk microphysics model. *J. Atmos. Sci.*, **74**, 2081–2104, https://doi.org/10.1175/JAS-D-16-0350.1.

——, ——, and ——, 2018: Microphysical characteristics of squall-line stratiform precipitation and transition zones simulated using an ice particle property-evolving model. *Mon. Wea. Rev.*, **146**, 723–743, https://doi.org/10.1175/MWR-D-17-0215.1.

Jin, H.-G., H. Lee, and J.-J. Baik, 2019: A new parameterization of the accretion of cloud water by graupel and its evaluation through cloud and precipitation simulations. *J. Atmos. Sci.*, **76**, 381–400, https://doi.org/10.1175/JAS-D-18-0245.1.

Kain, J. S., 2004: The Kain–Fritsch convective parameterization: An update. *J. Appl. Meteor.*, **43**, 170–181, https://doi.org/10.1175/1520-0450(2004)043<0170:TKCPAU>2.0.CO;2.

Khvorostyanov, V. I., and J. A. Curry, 2002: Terminal velocities of droplets and crystals: Power laws with continuous parameters over the size spectrum. *J. Atmos. Sci.*, **59**, 1872–1884, https://doi.org/10.1175/1520-0469(2002)059<1872:TVODAC>2.0.CO;2.

——, and ——, 2005: Fall velocities of hydrometeors in the atmosphere: Refinements to a continuous analytical power law. *J. Atmos. Sci.*, **62**, 4343–4357, https://doi.org/10.1175/JAS3622.1.

Lamb, D., and J. Verlinde, 2011: *Physics and Chemistry of Clouds*. Cambridge University Press, 584 pp.

Lee, H., and J.-J. Baik, 2017: A physically based autoconversion parameterization. *J. Atmos. Sci.*, **74**, 1599–1616, https://doi.org/10.1175/JAS-D-16-0207.1.

——, A. M. Fridlind, and A. S. Ackerman, 2019: An evaluation of size-resolved cloud microphysics scheme numerics for use with radar observations. Part I: Collision–coalescence. *J. Atmos. Sci.*, **76**, 247–263, https://doi.org/10.1175/JAS-D-18-0174.1.

Lim, K.-S. S., and S.-Y. Hong, 2010: Development of an effective double-moment cloud microphysics scheme with prognostic cloud condensation nuclei (CCN) for weather and climate models. *Mon. Wea. Rev.*, **138**, 1587–1612, https://doi.org/10.1175/2009MWR2968.1.

Lin, Y.-L., R. D. Farley, and H. D. Orville, 1983: Bulk parameterization of the snow field in a cloud model. *J. Climate Appl. Meteor.*, **22**, 1065–1092, https://doi.org/10.1175/1520-0450(1983)022<1065:BPOTSF>2.0.CO;2.

Locatelli, J. D., and P. V. Hobbs, 1974: Fall speeds and masses of solid precipitation particles. *J. Geophys. Res.*, **79**, 2185–2197, https://doi.org/10.1029/JC079i015p02185.

Milbrandt, J. A., and M. K. Yau, 2005: A multimoment bulk microphysics parameterization. Part II: A proposed three-moment closure and scheme description. *J. Atmos. Sci.*, **62**, 3065–3081, https://doi.org/10.1175/JAS3535.1.

——, and H. Morrison, 2016: Parameterization of cloud microphysics based on the prediction of bulk ice particle properties. Part III: Introduction of multiple free categories. *J. Atmos. Sci.*, **73**, 975–995, https://doi.org/10.1175/JAS-D-15-0204.1.

Mitchell, D. L., 1996: Use of mass- and area-dimensional power laws for determining precipitation particle terminal velocities. *J. Atmos. Sci.*, **53**, 1710–1723, https://doi.org/10.1175/1520-0469(1996)053<1710:UOMAAD>2.0.CO;2.

——, and A. J. Heymsfield, 2005: Refinements in the treatment of ice particle terminal velocities, highlighting aggregates. *J. Atmos. Sci.*, **62**, 1637–1644, https://doi.org/10.1175/JAS3413.1.

Mlawer, E. J., S. J. Taubman, P. D. Brown, M. J. Iacono, and S. A. Clough, 1997: Radiative transfer for inhomogeneous atmospheres: RRTM, a validated correlated-k model for the longwave. *J. Geophys. Res.*, **102**, 16 663–16 682, https://doi.org/10.1029/97JD00237.

Molthan, A. L., W. A. Petersen, S. W. Nesbitt, and D. Hudak, 2010: Evaluating the snow crystal size distribution and density assumptions within a single-moment microphysics scheme. *Mon. Wea. Rev.*, **138**, 4254–4267, https://doi.org/10.1175/2010MWR3485.1.

Morrison, H., and J. A. Milbrandt, 2011: Comparison of two-moment bulk microphysics schemes in idealized supercell thunderstorm simulations. *Mon. Wea. Rev.*, **139**, 1103–1130, https://doi.org/10.1175/2010MWR3433.1.

——, and ——, 2015: Parameterization of cloud microphysics based on the prediction of bulk ice particle properties. Part I: Scheme description and idealized tests. *J. Atmos. Sci.*, **72**, 287–311, https://doi.org/10.1175/JAS-D-14-0065.1.

——, A. A. Jensen, J. Y. Harrington, and J. A. Milbrandt, 2016: Advection of coupled hydrometeor quantities in bulk cloud microphysics schemes. *Mon. Wea. Rev.*, **144**, 2809–2829, https://doi.org/10.1175/MWR-D-15-0368.1.

NCEP, 2015: NCEP GDAS/FNL 0.25 degree global tropospheric analyses and forecast grids. NCAR Computational and Information Systems Laboratory Research Data Archive, accessed 18 September 2019, https://doi.org/10.5065/D65Q4T4Z.

Phillips, V. T. J., M. Formenton, A. Bansemer, I. Kudzotsa, and B. Lienert, 2015: A parameterization of sticking efficiency for collisions of snow and graupel with ice crystals: Theory and comparison with observations. *J. Atmos. Sci.*, **72**, 4885–4902, https://doi.org/10.1175/JAS-D-14-0096.1.

Seifert, A., U. Blahak, and R. Buhr, 2014: On the analytic approximation of bulk collision rates of non-spherical hydrometeors. *Geosci. Model Dev.*, **7**, 463–478, https://doi.org/10.5194/gmd-7-463-2014.

Skamarock, W. C., and Coauthors, 2008: A description of the Advanced Research WRF version 3. NCAR Tech. Note TN-475+STR, 113 pp., https://doi.org/10.5065/D68S4MVH.

Tewari, M., and Coauthors, 2004: Implementation and verification of the unified NOAH land surface model in the WRF Model. *20th Conf. on Weather Analysis and Forecasting/16th Conf. on Numerical Weather Prediction*, Seattle, WA, Amer. Meteor. Soc., 14.2a, https://ams.confex.com/ams/pdfpapers/69061.pdf.

Thompson, G., P. R. Field, R. M. Rasmussen, and W. D. Hall, 2008: Explicit forecasts of winter precipitation using an improved bulk microphysics scheme. Part II: Implementation of a new snow parameterization. *Mon. Wea. Rev.*, **136**, 5095–5115, https://doi.org/10.1175/2008MWR2387.1.

Verlinde, J., P. J. Flatau, and W. R. Cotton, 1990: Analytical solutions to the collection growth equation: Comparison with approximate methods and applications to cloud microphysics parameterization schemes. *J. Atmos. Sci.*, **47**, 2871–2880, https://doi.org/10.1175/1520-0469(1990)047<2871:ASTTCG>2.0.CO;2.

Wang, J., and K. P. Georgakakos, 2005: Effects of cold microphysical processes on the surface precipitation variability of nonsquall tropical oceanic convection. *J. Geophys. Res.*, **110**, D22203, https://doi.org/10.1029/2005JD005787.

Wang, P. K., and W. Ji, 2000: Collision efficiencies of ice crystals at low–intermediate Reynolds numbers colliding with supercooled cloud droplets: A numerical study. *J. Atmos. Sci.*, **57**, 1001–1009, https://doi.org/10.1175/1520-0469(2000)057<1001:CEOICA>2.0.CO;2.

Weisman, M. L., and J. B. Klemp, 1982: The dependence of numerically simulated convective storms on vertical wind shear and buoyancy. *Mon. Wea. Rev.*, **110**, 504–520, https://doi.org/10.1175/1520-0493(1982)110<0504:TDONSC>2.0.CO;2.

Wisner, C., H. D. Orville, and C. Myers, 1972: A numerical model of a hail-bearing cloud. *J. Atmos. Sci.*, **29**, 1160–1181, https://doi.org/10.1175/1520-0469(1972)029<1160:ANMOAH>2.0.CO;2.

Woods, C. P., M. T. Stoelinga, and J. D. Locatelli, 2008: Size spectra of snow particles measured in wintertime precipitation in the Pacific Northwest. *J. Atmos. Sci.*, **65**, 189–205, https://doi.org/10.1175/2007JAS2243.1.

Zhang, D.-L., and R. A. Anthes, 1982: A high-resolution model of the planetary boundary layer—Sensitivity tests and comparisons with SESAME-79 data. *J. Appl. Meteor.*, **21**, 1594–1609, https://doi.org/10.1175/1520-0450(1982)021<1594:AHRMOT>2.0.CO;2.